



Article

Interlayer Separation in Graphene Paper Comprising Electrochemically Exfoliated Graphene

Dang Du Nguyen ¹, TaeGyeong Lim ¹, Soomook Lim ¹ and Ji Won Suk ^{1,2,3,*}

¹ School of Mechanical Engineering, Sungkyunkwan University, Suwon 16419, Gyeonggi-do, Korea; dangdunguyen.bku@gmail.com (D.D.N.); taegyung95@gmail.com (T.L.); growing18@naver.com (S.L.)

² Department of Smart Fab. Technology, Sungkyunkwan University, Suwon 16419, Gyeonggi-do, Korea

³ SKKU Advanced Institute of Nanotechnology (SAINT), Sungkyunkwan University, Suwon 16419, Gyeonggi-do, Korea

* Correspondence: jwsuk@skku.edu

Abstract: The emergence of graphene paper comprising well-stacked graphene flakes has promoted the application of graphene-based materials in diverse fields such as energy storage devices, membrane desalination, and actuators. The fundamental properties of graphene paper such as mechanical, electrical, and thermal properties are critical to the design and fabrication of paper-based devices. In this study, the interlayer interactions in graphene paper were investigated by double cantilever beam (DCB) fracture tests. Graphene papers fabricated by flow-directed stacking of electrochemically exfoliated few-layer graphene flakes were mechanically separated into two parts, which generated force-displacement responses of the DCB sample. The analysis based on fracture mechanics revealed that the interlayer separation energy of the graphene paper was 9.83 ± 0.06 J/m². The results provided a fundamental understanding of the interfacial properties of graphene papers, which will be useful for developing paper-based devices with mechanical integrity.

Keywords: graphene paper; electrochemical exfoliation; interlayer separation; fracture; double cantilever beam



Citation: Nguyen, D.D.; Lim, T.; Lim, S.; Suk, J.W. Interlayer Separation in Graphene Paper Comprising Electrochemically Exfoliated Graphene. *Nanomaterials* **2021**, *11*, 865. <https://doi.org/10.3390/nano11040865>

Academic Editor: Christophe Donnet

Received: 20 February 2021

Accepted: 24 March 2021

Published: 29 March 2021

Publisher's Note: MDPI stays neutral with regard to jurisdictional claims in published maps and institutional affiliations.



Copyright: © 2021 by the authors. Licensee MDPI, Basel, Switzerland. This article is an open access article distributed under the terms and conditions of the Creative Commons Attribution (CC BY) license (<https://creativecommons.org/licenses/by/4.0/>).

1. Introduction

Graphene has attracted considerable interest from researchers in academia and industry owing to its exceptional mechanical, electrical, optical, and thermal properties [1–5]. These properties facilitate the utilization of graphene in various advanced applications, such as energy storage devices, nanoelectronics, optoelectronics, nanocomposites, and flexible devices [6–12]. High-quality and stable single-layer graphene on SiO₂ can be obtained via the mechanical exfoliation of bulk graphite using scotch tape [1]. However, this technique is not suitable for mass production due to various issues such as low lateral sizes and random positions of the graphene flakes; in addition, it is difficult to control the number of layers of the graphene flakes. Therefore, several methods have been developed for the production of graphene in substantial quantities, such as epitaxial growth on SiC [13], chemical vapor deposition (CVD) on metal substrates [14], and oxidation of graphite followed by reduction of graphene oxide (GO) [15]. The oxidation of graphite, subsequent exfoliation of graphite oxide to GO, and eventual chemical or thermal reduction of GO is a scalable and inexpensive technique to obtain substantial quantities of graphene flakes [16]. GO and reduced graphene oxide (rGO) have been extensively utilized as components of paper-like materials [17,18], nanocomposites [15,19], electrodes for energy storage devices [20,21], transparent conducting films [22], and high-performance coatings [23]. However, the oxidation of graphite induces the formation of numerous defects and oxygen functional groups [24]. The direct exfoliation of graphite using electrochemical exfoliation, without the involvement of hazardous chemicals, is a viable alternative to the use of colloidal suspensions of GO [25,26]. Electrochemically exfoliated graphene (EEG) exhibits a high

C/O atomic ratio and minimal defects. Therefore, it has been extensively utilized in various applications, such as electrodes of supercapacitors and batteries, field-effect transistors, conductive fillers in polymer composites, and conductive inks [25–33].

Macroscopic paper-like materials, among the multiple applications of graphene-based materials, exhibit high potential for utilization in free-standing, lightweight, and flexible devices, such as energy storage devices, membranes, sensors, and actuators [34,35]. Mechanical integrity is a fundamental property of graphene papers, and it is crucial for the development of reliable and high-performance paper-based devices. Graphene papers are formed by layer-by-layer assembly; therefore, the interlayer interaction significantly influences the mechanical properties of these papers. There has been extensive research on strengthening the interactions between the graphene layers to increase the fracture strengths and Young's moduli of graphene papers. It has been reported that the mechanical properties of GO papers can be enhanced by chemical cross-linking using divalent metal ions [36]. A decrease in the interlayer spacing of EEG paper strengthens the interlayer interactions, thereby increasing the fracture strength of graphene papers [37]. However, there is limited knowledge about the interlayer interactions in graphene papers.

In this work, the interlayer separation in graphene paper was investigated using mode I fracture tests. Graphene flakes were obtained using electrochemical exfoliation of graphite; subsequently, graphene papers were fabricated by flow-directed assembly of the obtained graphene flakes. The double cantilever beam (DCB) specimens for the mode I fracture tests were prepared by gluing both sides of the graphene paper to two Si substrates. The interlayer separation energy was estimated using the force–displacement responses obtained from the mechanical separation of the graphene paper.

2. Materials and Methods

2.1. Fabrication of Graphene Papers Using EEG Flakes

Graphene flakes were synthesized by the electrochemical exfoliation of graphite (Supplementary Figure S1a) [38]. A commercial graphite foil (99.8% purity (metal basis); Alfa Aesar, Haverhill, MA, USA) with a thickness of 0.5 mm was cut into 5 cm-long and 1 cm-wide strips for application as a working electrode (Supplementary Figure S2a). A Pt plate was utilized as a counter electrode and placed parallel to the graphite electrode at a fixed distance of 2 cm [39]. A 0.1 M electrolyte solution was prepared by the dissolution of ammonium sulfate ($(\text{NH}_4)_2\text{SO}_4$; Sigma-Aldrich, St. Louis, MO, USA) in water and subsequent stirring at 100 rpm for 10 min. Electrochemical exfoliation was initiated by applying a DC voltage (2 V) to the graphite for 3 min. This facilitated wetting of the graphite electrode and intercalation of the electrolyte anions that induced lattice expansion in graphite. Exfoliation was completed under an applied voltage of 10 V. Thereafter, the suspended graphene sheets were collected using vacuum filtration through a polytetrafluoroethylene (PTFE) membrane filter (pore size = 0.2 μm) and washed several times with ethanol and deionized water (Supplementary Figure S1b). This was followed by drying in an oven for 12 h at 60 °C to remove the moisture in the powders. The dried graphene powders were dispersed in dimethylformamide (DMF) by sonication for 30 min. The EEG suspension was subjected to centrifugation at 3000 rpm for 30 min to remove the thick graphene flakes. Graphene papers were fabricated by vacuum filtration of the EEG dispersion (0.15 mg/mL in DMF, Supplementary Figure S2b) using an anodic aluminum oxide (AAO) membrane filter (pore size = 0.2 μm ; Whatman, Maidstone, UK).

2.2. Characterization of EEG Paper

The EEG papers were subjected to morphological analysis using scanning electron microscopy (SEM; JSM-7600, Jeol Ltd., Tokyo, Japan). The EEG flakes were placed on a SiO_2/Si substrate; thereafter, their lateral sizes and thicknesses were determined using SEM and atomic force microscopy (AFM; 5300E, Hitachi High-Technologies Corporation, Tokyo, Japan), respectively. The EEG papers and their fracture surfaces were characterized by Raman spectroscopy (alpha300M, WITec GmbH, Ulm, Germany) with a laser

wavelength of 532 nm. The chemical structures of the EEG papers were characterized using Fourier-transform infrared (FTIR) spectroscopy (IFS-66/S, Tensor 27, Bruker Optik GmbH, Ettlingen, Germany) and X-ray photoelectron spectroscopy (XPS; Escalab-250 (with monochromated Al K α radiation), Thermo Fisher Scientific, Waltham, MA, USA). The C 1s peak of the XPS spectra was deconvoluted using Gaussian–Lorentzian peak shapes after Shirley background correction [40]. The crystalline structures of the EEG papers were characterized by X-ray diffraction (XRD; D8 Advance, Bruker AXS GmbH, Karlsruhe, Germany) using Cu K α radiation. Thermogravimetric analysis (TGA; EXSTAR TG/DTA6100, Seiko Instruments Inc., Chiba, Japan) was performed at a temperature range of 25–600 °C under nitrogen atmosphere. The electrical conductivity of the EEG paper was measured by the van der Pauw method with four-point probes.

2.3. Interlayer Separation in EEG Paper

The DCB specimens (5 × 30 mm) were prepared by sandwiching the EEG paper between two Si substrates using a high-viscosity adhesive (302/80Z, Epoxy Technology, MA, USA). The prepared DCB specimens exhibited a configuration of Si/adhesive/graphene paper/adhesive/Si (Supplementary Figure S3a). The laminated samples were cured at 100 °C for 2 h, and Al loading tabs were attached to one side of each Si substrate for the application of a tensile force.

Glue was not applied at one end of the substrate, where the loading tabs were attached, to allow the formation of an initial crack. The initial crack length (a_0) was determined from the distance between the center point of the loading tab and the crack front. The DCB specimens were mechanically separated by mode I fracture tests at a constant displacement rate of 0.5 mm/min using a universal testing machine (QC-506M2, Cometech, Taiwan) (Supplementary Figure S3b). The crack length (a) at any point during the DCB fracture test was estimated from the force–displacement responses using simple beam theory, according to the following equation [41,42]:

$$a^3 = Ebh^3\Delta/8P, \quad (1)$$

where P and Δ represent the load and applied displacement, respectively; furthermore, E , b , and h denote the in-plane Young's modulus, width, and thickness of the substrate, respectively. The interlayer separation energy of the graphene paper was determined from the energy release rate (G) obtained using the following equation [41,42]:

$$G = 12a^2P^2/Eh^3b^2, \quad (2)$$

3. Results and Discussion

3.1. Characterization of EEG Papers

The EEG flakes were dispersed on a SiO₂/Si substrate, and their lateral sizes were estimated from the SEM images (Figure 1a). Most of the flakes exhibited sizes of less than approximately 3 μ m (Figure 1b). The AFM observations revealed that the EEG flakes comprised a few layers (Figure 1c). The thickness of the EEG flakes was determined to be approximately 1–1.5 nm based on the line profiles presented in Figure 1d. These results indicated that the morphologies of the EEG flakes in this study were similar to those of the previously reported EEG flakes on an SiO₂ substrate [32]. The EEG paper, obtained by vacuum filtration, exhibited uniform and smooth surfaces with negligible wrinkles (Figure 1e). The cross-sectional SEM image in Figure 1f confirmed the layer-by-layer stacking of the EEG flakes in the paper (thickness = 19.6 ± 1.4 μ m).

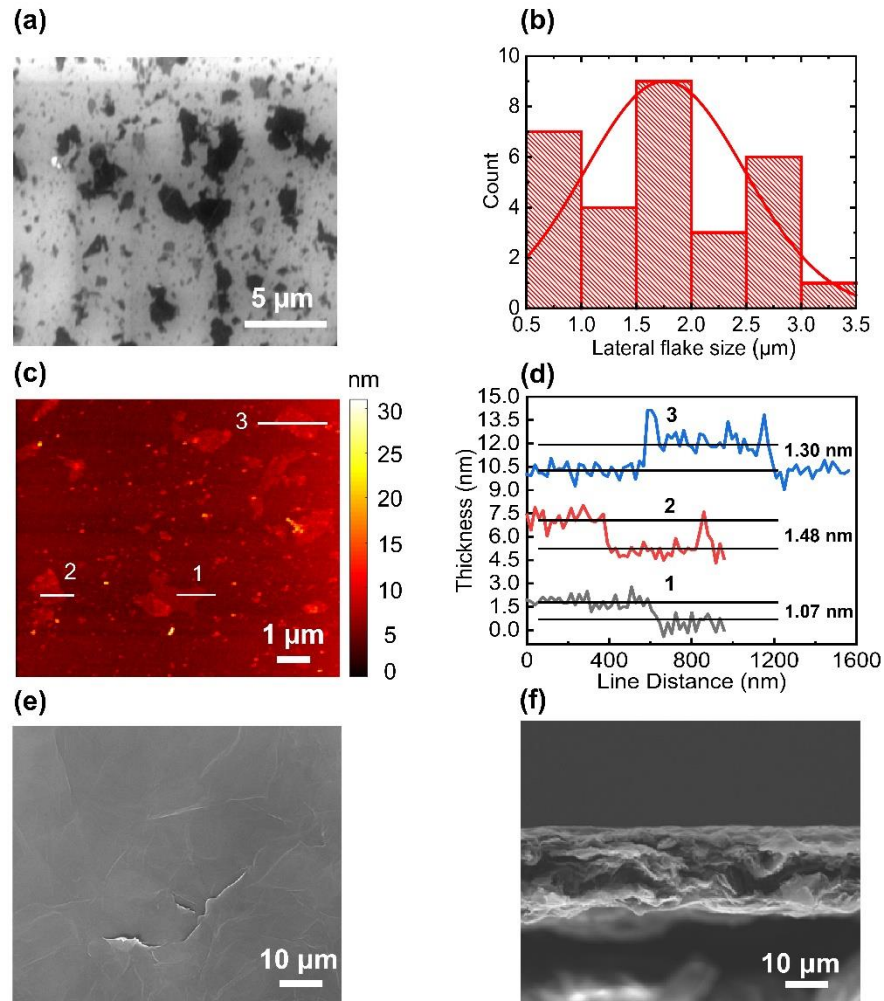


Figure 1. Morphologies of the EEG flakes and papers: (a) SEM image of the EEG flakes placed on an SiO₂/Si substrate; (b) histogram of the lateral sizes of the EEG flakes, estimated from the SEM image (the red solid lines represent the Gaussian fits to the data); (c) AFM image of the EEG flakes placed on an SiO₂/Si substrate; (d) representative AFM line profiles of the EEG flakes; (e) SEM image of the surface morphology of the EEG paper; (f) cross-sectional SEM image of the EEG paper.

The interlayer structure of the EEG paper was characterized by thin-film XRD analysis. The XRD pattern of the EEG paper exhibited a prominent peak at 26.46° corresponding to a d-spacing of 0.3364 nm (Figure 2a). The XRD pattern of a graphite foil is also presented in Figure 2a, and it exhibited a peak at 26.58° corresponding to a d-spacing of 0.3349 nm. The slightly higher d-spacing of the EEG paper than that of the graphite foil was attributed to the presence of oxygen functional groups generated by electrochemical exfoliation [25,32]. The Raman spectrum of the EEG paper depicted the characteristic features of the graphene flakes (Figure 2b). The D band, G band, and 2D band were observed at approximately 1352, 1584, and 2680 cm⁻¹, respectively. The D band corresponded to defects such as functional groups or structural disorders in the sp² carbon network of the EEG flakes. The peak intensity ratio of the D band to the G band, i.e., I_D/I_G, for the EEG paper (1.08) was similar to that for chemically or thermally reduced GO flakes (~1.2–1.5) [43,44].

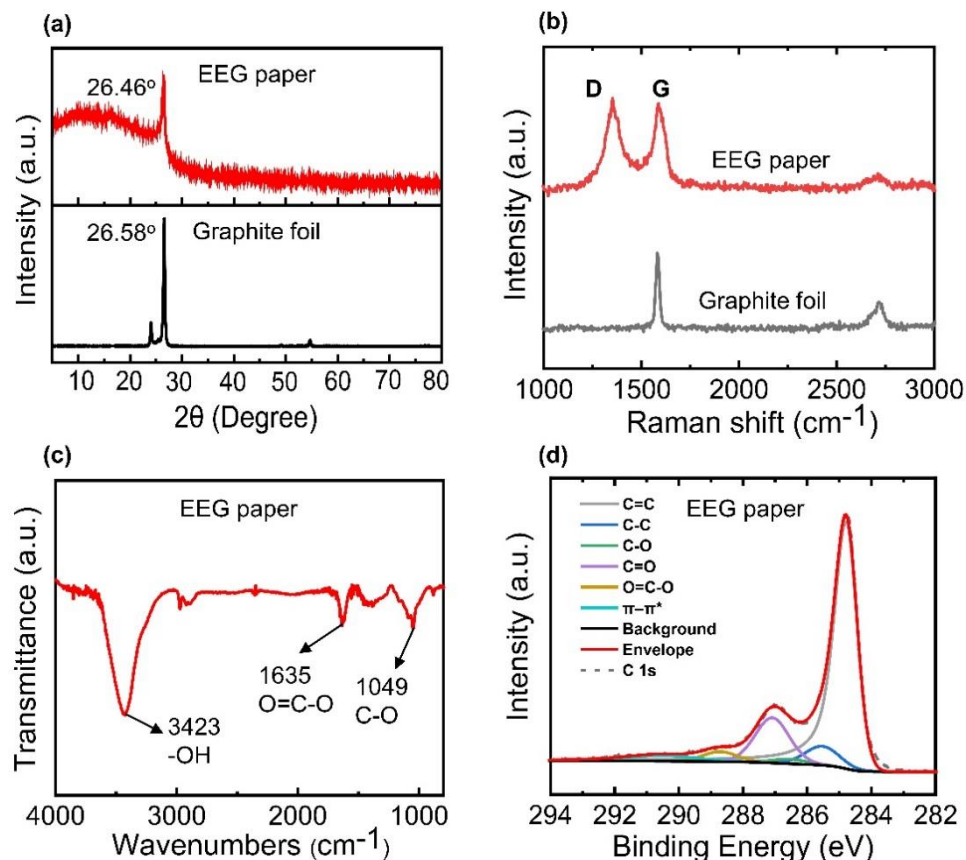


Figure 2. (a) XRD patterns and (b) Raman spectra of a graphite foil and the EEG paper; (c) FTIR spectrum and (d) XPS C 1s core-level spectrum of the EEG paper.

The results of FTIR spectroscopy indicated the presence of oxygen functional groups in the EEG flakes (Figure 2c). The characteristic peaks in the FTIR spectrum at 3423, 1635, and 1049 cm^{-1} corresponded to the hydroxyl, carboxyl, and alkoxy groups, respectively [45–47]. The chemical structure of the EEG paper was investigated by XPS. The C 1s spectrum was fitted with six spectral components corresponding to C=C, C-C, C-O, C=O, O=C-O, and a π - π^* shake-up at 284.8, 285.5, 286.5, 287.1, 288.7, and 290.5 eV, respectively [39,48–51]. The C/O atomic ratio of EEG (~3.4), obtained by XPS analysis, was higher than that of GO [52–54]. However, the C/O ratio was relatively lower than those of other graphene flakes synthesized by the electrochemical exfoliation method, which might be attributed to more oxidation during the exfoliation process [55]. Moreover, TGA on the EEG paper showed the weight loss associated with the thermal removal of the oxygen functional groups in the paper (Supplementary Figure S4) [55]. In addition, the EEG paper exhibited a relatively lower electrical conductivity of 2570 ± 980 S/m compared to those of other graphene papers, which is consistent with the lower C/O ratio of the EEG paper [56].

3.2. Interlayer Separation in the EEG Paper Using Mode I Fracture

The EEG paper was subjected to mode I fracture to elucidate the interlayer interactions between the graphene flakes. The photographs of the upper and lower Si substrates (USi and LSi) after the fracture showed the uniform dark color of the entire substrate (Figure 3a). This indicated the complete coverage of the EEG flakes over the adhesive on the Si substrates. The SEM image of the USi revealed the presence of the EEG paper in the epoxy region (Figure 3b). The complementary fracture surface of the EEG paper was observed in the left region of the LSi, while the original EEG paper was observed in the right region of the LSi (Figure 3d). This was attributed to the absence of epoxy in the right region of the USi. The Raman intensity maps of the D band (1310 – 1390 cm^{-1}) revealed the presence of EEG flakes near the epoxy terminus (Figure 3c,e). The entire

fracture surfaces of the USi and LSi were subjected to SEM observations and Raman mapping. The results confirmed the uniform separation of the EEG paper into the USi and LSi (Supplementary Figures S5–S7).

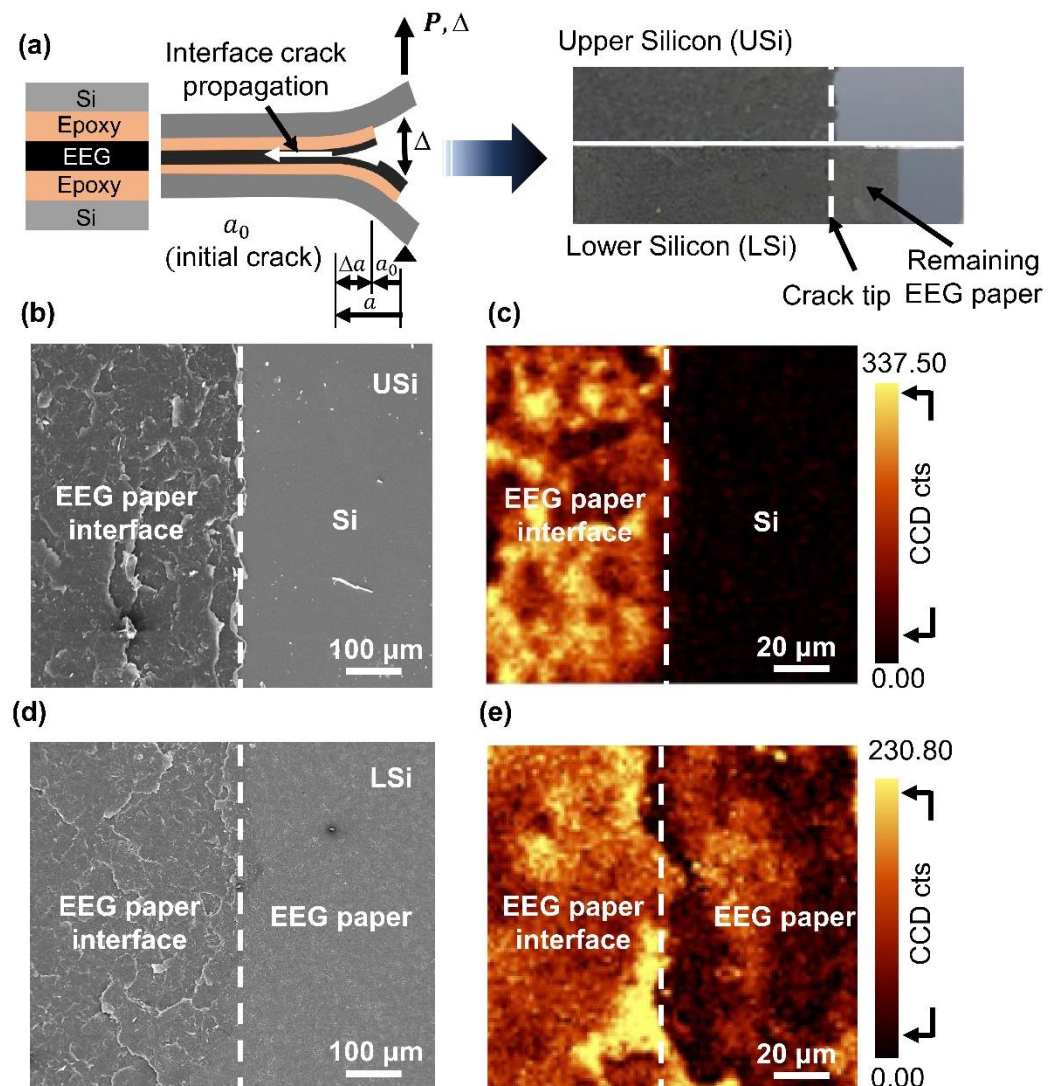


Figure 3. Characterization of the fracture surface of the EEG paper after the mode I fracture test: (a) schematic illustration of the interlayer separation in the EEG paper and a photograph of the DCB specimen after fracture; (b,d) SEM images and (c,e) Raman intensity maps of the D band for the fracture surfaces of the USi and LSi near the epoxy terminus.

Figure 4a presents the force–displacement responses for the interlayer separation in the EEG paper. When the specimen was subjected to monotonic loading, there was a linear increase in the force before the occurrence of fracture. A sudden decrease in the force indicated crack initiation corresponding to the interlayer separation in the EEG paper. There was an overall decrease in the force owing to crack propagation. The similar force–displacement curves and uniform fracture surfaces of the three specimens indicated the excellent repeatability of the measurements (Figure 4c,e). The interlayer separation energy of the EEG paper was estimated from the force–displacement responses based on the concept of linear elastic fracture mechanics. The J-integral (J), determined from the energy release rate (G), represented the interlayer bonding energy of the EEG paper (Figure 4b). The interlayer separation energy of the three specimens was determined to be $9.83 \pm 0.06 \text{ J/m}^2$ (Figure 4d), as depicted by the red dashed line in Figure 4b. The interlayer

separation energy of the EEG paper was higher than the adhesion energies for previously reported graphene-based systems. The adhesion energy between monolayer graphene, obtained by mechanical exfoliation, and an SiO₂ substrate was reported to be 0.45 J/m² [57]. The adhesion energy between monolayer graphene, synthesized by CVD, and a seed Cu foil was reported to be 6 J/m² [41], while that between graphene and highly oriented pyrolytic graphite was reported to be 0.088 J/m² [58]. The adhesion energy between graphite and a diamond tip was reported to be 0.0259–0.1871 J/m² [59]. The high interlayer separation energy of the EEG paper was attributed to the oxygen functional groups in the EEG flakes that induced strong layer-to-layer interactions [60]. The layer-by-layer assembly of the EEG paper resulted in a microstructure comprising interlocked EEG flakes, and this also contributed to the high interfacial cohesion energy [37]. Therefore, the energy required for interlayer separation was higher for the EEG paper than that for other two-dimensional materials [61,62].

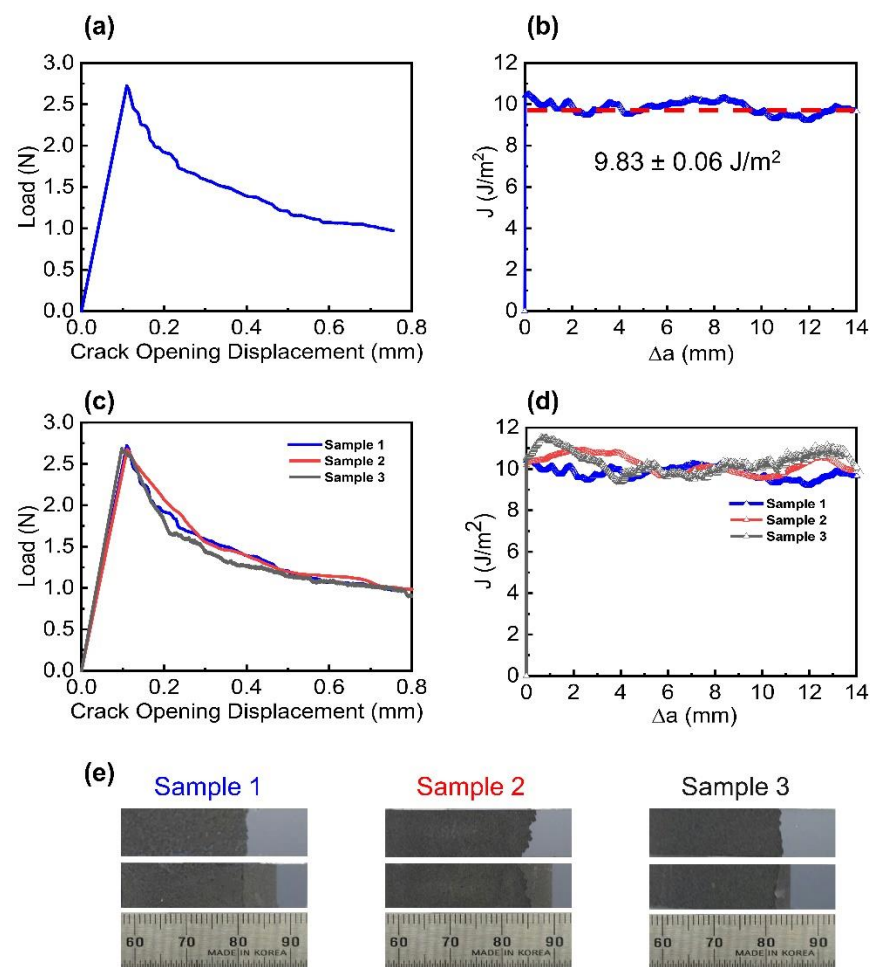


Figure 4. Interlayer separation behavior of the EEG paper: (a) force–displacement responses and (b) corresponding fracture resistance curve; (c) force–displacement curves and (d) corresponding fracture resistance curves of the three DCB specimens. Interfacial fracture behavior of the interface of the EEG paper. The red dashed line in (b) represents the average interlayer separation energy obtained from (d); (e) photograph of the fracture surfaces of the three DCB specimens.

4. Conclusions

Mechanical integrity of graphene papers is important for developing reliable paper-based devices. In this study, a classical fracture test was performed to induce interlayer separation in graphene paper, and the interlayer interactions between the graphene flakes were elucidated. Graphene flakes were obtained by electrochemical exfoliation of graphite;

thereafter, graphene papers were fabricated via vacuum filtration of the obtained graphene flakes. The mode I fracture tests successfully separated the EEG paper into two parts; SEM and Raman spectroscopy observation on the fracture surfaces confirmed a complete separation of the paper. Therefore, the force–displacement responses obtained from the fracture tests revealed the interlayer separation energy in the EEG paper of 9.83 ± 0.06 J/m². Since the EEG flakes were oxidized during the exfoliation process, the high separation energy was attributed to the strong interactions induced by the oxygen functional groups in the flakes. Furthermore, the interlocking of the individual EEG flakes in the paper might be another reason for the high separation energy. A better understanding of the interlayer interactions in graphene paper will facilitate the development of paper-based devices.

Supplementary Materials: The followings are available online at <https://www.mdpi.com/article/10.3390/nano11040865/s1>, Figure S1: Schematic illustration of the fabrication of the EEG paper; Figure S2: Photograph of (a) graphite foils and (b) dispersed EEG flakes in DMF; Figure S3: Schematic illustration of the mode I fracture tests of the EEG paper; Figure S4: TGA curve of the EEG paper; Figure S5: SEM images of the fracture surfaces of the upper and lower Si strips after the fracture tests; Figure S6: Raman spectra of the EEG paper after fracture; Figure S7: Raman intensity maps of the D band and G band for the fracture surface.

Author Contributions: Conceptualization, J.W.S.; formal analysis, D.D.N.; investigation, D.D.N., T.L. and S.L.; data curation, D.D.N.; writing—original draft preparation, D.D.N. and J.W.S.; writing—review and editing, J.W.S.; visualization, D.D.N.; supervision, J.W.S.; project administration, J.W.S.; funding acquisition, J.W.S. All authors have read and agreed to the published version of the manuscript.

Funding: This study was supported by the Basic Research Program through the National Research Foundation of Korea (NRF) grant funded by the Ministry of Science and ICT (No. 2019R1A2C2089785). The work was also supported by the Korea Electric Power Corporation (No. R19XO01-16).

Institutional Review Board Statement: Not applicable.

Informed Consent Statement: Not applicable.

Data Availability Statement: Not applicable.

Conflicts of Interest: The authors declare no conflict of interest.

References

1. Novoselov, K.S.; Geim, A.K.; Morozov, S.V.; Jiang, D.; Zhang, Y.; Dubonos, S.V.; Grigorieva, I.V.; Firsov, A.A. Electric field effect in atomically thin carbon films. *Science* **2004**, *306*, 666–669. [[CrossRef](#)] [[PubMed](#)]
2. Lee, C.; Wei, X.; Kysar, J.W.; Hone, J. Measurement of the elastic properties and intrinsic strength of monolayer graphene. *Science* **2008**, *321*, 385–388. [[CrossRef](#)] [[PubMed](#)]
3. Bolotin, K.I.; Sikes, K.J.; Jiang, Z.; Klima, M.; Fudenberg, G.; Hone, J.; Kim, P.; Stormer, H. Ultrahigh electron mobility in suspended graphene. *Solid State Commun.* **2008**, *146*, 351–355. [[CrossRef](#)]
4. Bonaccorso, F.; Sun, Z.; Hasan, T.; Ferrari, A. Graphene photonics and optoelectronics. *Nat. Photonics* **2010**, *4*, 611. [[CrossRef](#)]
5. Lee, D.; Lee, S.; An, B.-S.; Kim, T.-H.; Yang, C.-W.; Suk, J.W.; Baik, S. Dependence of the In-Plane Thermal Conductivity of Graphene on Grain Misorientation. *Chem. Mater.* **2017**, *29*, 10409–10417. [[CrossRef](#)]
6. Bonaccorso, F.; Colombo, L.; Yu, G.; Stoller, M.; Tozzini, V.; Ferrari, A.C.; Ruoff, R.S.; Pellegrini, V. Graphene, related two-dimensional crystals, and hybrid systems for energy conversion and storage. *Science* **2015**, *347*, 1246501. [[CrossRef](#)]
7. Avouris, P. Graphene: Electronic and Photonic Properties and Devices. *Nano Lett.* **2010**, *10*, 4285–4294. [[CrossRef](#)]
8. Young, R.J.; Kinloch, I.A.; Gong, L.; Novoselov, K.S. The mechanics of graphene nanocomposites: A review. *Compos. Sci. Technol.* **2012**, *72*, 1459–1476. [[CrossRef](#)]
9. Kim, H.; Ahn, J.-H. Graphene for flexible and wearable device applications. *Carbon* **2017**, *120*, 244–257. [[CrossRef](#)]
10. Jiang, L.; Yuan, C.; Li, Z.; Su, J.; Yi, Z.; Yao, W.; Wu, P.; Liu, Z.; Cheng, S.; Pan, M. Multi-band and high-sensitivity perfect absorber based on monolayer graphene metamaterial. *Diam. Relat. Mater.* **2021**, *111*, 108227. [[CrossRef](#)]
11. Qi, Y.; Zhang, Y.; Liu, C.; Zhang, T.; Zhang, B.; Wang, L.; Deng, X.; Bai, Y.; Wang, X. A tunable terahertz metamaterial absorber composed of elliptical ring graphene arrays with refractive index sensing application. *Results Phys.* **2020**, *16*, 103012. [[CrossRef](#)]
12. Ahmadivand, A.; Gerislioglu, B.; Ramezani, Z. Gated graphene island-enabled tunable charge transfer plasmon terahertz metamodulator. *Nanoscale* **2019**, *11*, 8091–8095. [[CrossRef](#)]
13. Berger, C.; Song, Z.; Li, X.; Wu, X.; Brown, N.; Naud, C.; Mayou, D.; Li, T.; Hass, J.; Marchenkov, A.N.; et al. Electronic Confinement and Coherence in Patterned Epitaxial Graphene. *Science* **2006**, *312*, 1191–1196. [[CrossRef](#)]

14. Li, X.; Cai, W.; An, J.; Kim, S.; Nah, J.; Yang, D.; Piner, R.; Velamakanni, A.; Jung, I.; Tutuc, E.; et al. Large-Area Synthesis of High-Quality and Uniform Graphene Films on Copper Foils. *Science* **2009**, *324*, 1312–1314. [[CrossRef](#)]
15. Stankovich, S.; Dikin, D.A.; Dommett, G.H.B.; Kohlhaas, K.M.; Zimney, E.J.; Stach, E.A.; Piner, R.D.; Nguyen, S.T.; Ruoff, R.S. Graphene-based composite materials. *Nature* **2006**, *442*, 282–286. [[CrossRef](#)]
16. Dreyer, D.R.; Park, S.; Bielawski, C.W.; Ruoff, R.S. The chemistry of graphene oxide. *Chem. Soc. Rev.* **2010**, *39*, 228–240. [[CrossRef](#)]
17. Park, S.; An, J.; Suk, J.W.; Ruoff, R.S. Graphene-Based Actuators. *Small* **2010**, *6*, 210–212. [[CrossRef](#)]
18. Dikin, D.A.; Stankovich, S.; Zimney, E.J.; Piner, R.D.; Dommett, G.H.B.; Evmenenko, G.; Nguyen, S.T.; Ruoff, R.S. Preparation and characterization of graphene oxide paper. *Nature* **2007**, *448*, 457–460. [[CrossRef](#)]
19. Vo, T.T.; Lee, H.-J.; Kim, S.-Y.; Suk, J.W. Synergistic Effect of Graphene/Silver Nanowire Hybrid Fillers on Highly Stretchable Strain Sensors Based on Spandex Composites. *Nanomaterials* **2020**, *10*, 2063. [[CrossRef](#)]
20. Stoller, M.D.; Park, S.; Zhu, Y.; An, J.; Ruoff, R.S. Graphene-Based Ultracapacitors. *Nano Lett.* **2008**, *8*, 3498–3502. [[CrossRef](#)]
21. Lim, T.; Ho, B.T.; Suk, J.W. High-performance and thermostable wire supercapacitors using mesoporous activated graphene deposited on continuous multilayer graphene. *J. Mater. Chem. A* **2021**, *9*, 4800–4809. [[CrossRef](#)]
22. Becerril, H.A.; Mao, J.; Liu, Z.; Stoltenberg, R.M.; Bao, Z.; Chen, Y. Evaluation of Solution-Processed Reduced Graphene Oxide Films as Transparent Conductors. *ACS Nano* **2008**, *2*, 463–470. [[CrossRef](#)]
23. Piao, C.; Jang, H.; Lim, T.; Kim, H.; Choi, H.R.; Hao, Y.; Suk, J.W. Enhanced dynamic performance of twisted and coiled soft actuators using graphene coating. *Compos. Part B Eng.* **2019**, *178*, 107499. [[CrossRef](#)]
24. Eigler, S.; Hirsch, A. Chemistry with graphene and graphene oxide—challenges for synthetic chemists. *Angew. Chem. Int. Ed.* **2014**, *53*, 7720–7738. [[CrossRef](#)]
25. Parvez, K.; Li, R.; Puniredd, S.R.; Hernandez, Y.; Hinkel, F.; Wang, S.; Feng, X.; Müllen, K. Electrochemically exfoliated graphene as solution-processable, highly conductive electrodes for organic electronics. *ACS Nano* **2013**, *7*, 3598–3606. [[CrossRef](#)]
26. Liu, N.; Luo, F.; Wu, H.; Liu, Y.; Zhang, C.; Chen, J. One-step ionic-liquid-assisted electrochemical synthesis of ionic-liquid-functionalized graphene sheets directly from graphite. *Adv. Funct. Mater.* **2008**, *18*, 1518–1525. [[CrossRef](#)]
27. Yu, P.; Lowe, S.E.; Simon, G.P.; Zhong, Y.L. Electrochemical exfoliation of graphite and production of functional graphene. *Curr. Opin. Colloid Interface Sci.* **2015**, *20*, 329–338. [[CrossRef](#)]
28. Lee, J.H.; Shin, D.W.; Makotchenko, V.G.; Nazarov, A.S.; Fedorov, V.E.; Kim, Y.H.; Choi, J.Y.; Kim, J.M.; Yoo, J.B. One-step exfoliation synthesis of easily soluble graphite and transparent conducting graphene sheets. *Adv. Mater.* **2009**, *21*, 4383–4387. [[CrossRef](#)]
29. Su, C.-Y.; Lu, A.-Y.; Xu, Y.; Chen, F.-R.; Khlobystov, A.N.; Li, L.-J. High-quality thin graphene films from fast electrochemical exfoliation. *ACS Nano* **2011**, *5*, 2332–2339. [[CrossRef](#)]
30. Shinde, D.B.; Debgupta, J.; Kushwaha, A.; Aslam, M.; Pillai, V.K. Electrochemical unzipping of multi-walled carbon nanotubes for facile synthesis of high-quality graphene nanoribbons. *J. Am. Chem. Soc.* **2011**, *133*, 4168–4171. [[CrossRef](#)]
31. Munuera, J.; Paredes, J.; Villar-Rodil, S.; Ayán-Varela, M.; Martínez-Alonso, A.; Tascón, J. Electrolytic exfoliation of graphite in water with multifunctional electrolytes: En route towards high quality, oxide-free graphene flakes. *Nanoscale* **2016**, *8*, 2982–2998. [[CrossRef](#)] [[PubMed](#)]
32. Parvez, K.; Wu, Z.-S.; Li, R.; Liu, X.; Graf, R.; Feng, X.; Müllen, K. Exfoliation of graphite into graphene in aqueous solutions of inorganic salts. *J. Am. Chem. Soc.* **2014**, *136*, 6083–6091. [[CrossRef](#)] [[PubMed](#)]
33. Liu, Z.; Wu, Z.S.; Yang, S.; Dong, R.; Feng, X.; Müllen, K. Ultraflexible in-plane micro-supercapacitors by direct printing of solution-processable electrochemically exfoliated graphene. *Adv. Mater.* **2016**, *28*, 2217–2222. [[CrossRef](#)] [[PubMed](#)]
34. Zhang, M.; Hou, C.; Halder, A.; Wang, H.; Chi, Q. Graphene papers: Smart architecture and specific functionalization for biomimetics, electrocatalytic sensing and energy storage. *Mater. Chem. Front.* **2017**, *1*, 37–60. [[CrossRef](#)]
35. Karthick, R.; Chen, F. Free-standing graphene paper for energy application: Progress and future scenarios. *Carbon* **2019**, *150*, 292–310. [[CrossRef](#)]
36. Park, S.; Lee, K.-S.; Bozoklu, G.; Cai, W.; Nguyen, S.T.; Ruoff, R.S. Graphene Oxide Papers Modified by Divalent Ions—Enhancing Mechanical Properties via Chemical Cross-Linking. *ACS Nano* **2008**, *2*, 572–578. [[CrossRef](#)] [[PubMed](#)]
37. Cao, T.; Liu, X.; Cheng, X.; Li, Y.; Sang, L.; Ma, J.; Wang, J.; He, J.; Wang, M.; Zhang, Y. Unveiling the thickness-dependent mechanical properties of graphene papers by in situ SEM tension. *RSC Adv.* **2019**, *9*, 4609–4615. [[CrossRef](#)]
38. Liu, F.; Wang, C.; Sui, X.; Riaz, M.A.; Xu, M.; Wei, L.; Chen, Y. Synthesis of graphene materials by electrochemical exfoliation: Recent progress and future potential. *Carbon Energy* **2019**, *1*, 173–199. [[CrossRef](#)]
39. Yang, S.; Brüller, S.; Wu, Z.-S.; Liu, Z.; Parvez, K.; Dong, R.; Richard, F.; Samorì, P.; Feng, X.; Müllen, K. Organic radical-assisted electrochemical exfoliation for the scalable production of high-quality graphene. *J. Am. Chem. Soc.* **2015**, *137*, 13927–13932. [[CrossRef](#)]
40. Suk, J.W.; Murali, S.; An, J.; Ruoff, R.S. Mechanical measurements of ultra-thin amorphous carbon membranes using scanning atomic force microscopy. *Carbon* **2012**, *50*, 2220–2225. [[CrossRef](#)]
41. Na, S.R.; Suk, J.W.; Tao, L.; Akinwande, D.; Ruoff, R.S.; Huang, R.; Liechti, K.M. Selective mechanical transfer of graphene from seed copper foil using rate effects. *ACS Nano* **2015**, *9*, 1325–1335. [[CrossRef](#)]
42. Xu, C.; Yang, T.; Kang, Y.; Li, Q.; Xue, T.; Liechti, K.M.; Huang, R.; Qiu, W. Rate-Dependent Decohesion Modes in Graphene-Sandwiched Interfaces. *Adv. Mater. Interfaces* **2019**, *6*, 1901217. [[CrossRef](#)]

43. Mattevi, C.; Eda, G.; Agnoli, S.; Miller, S.; Mkhoyan, K.A.; Celik, O.; Mastrogiovanni, D.; Granozzi, G.; Garfunkel, E.; Chhowalla, M. Evolution of electrical, chemical, and structural properties of transparent and conducting chemically derived graphene thin films. *Adv. Funct. Mater.* **2009**, *19*, 2577–2583. [[CrossRef](#)]
44. López, V.; Sundaram, R.S.; Gómez-Navarro, C.; Olea, D.; Burghard, M.; Gómez-Herrero, J.; Zamora, F.; Kern, K. Chemical Vapor Deposition Repair of Graphene Oxide: A Route to Highly-Conductive Graphene Monolayers. *Adv. Mater.* **2009**, *21*, 4683–4686. [[CrossRef](#)]
45. Mao, X.; Zhu, L.; Liu, H.; Chen, H.; Ju, P.; Li, W. Synthesis of graphene via electrochemical exfoliation in different electrolytes for direct electrodeposition of a Cu/graphene composite coating. *RSC Adv.* **2019**, *9*, 35524–35531. [[CrossRef](#)]
46. Tang, B.; Zhang, L.; Li, R.; Wu, J.; Hedhili, M.N.; Wang, P. Are vacuum-filtrated reduced graphene oxide membranes symmetric? *Nanoscale* **2016**, *8*, 1108–1116. [[CrossRef](#)]
47. Yang, E.; Ham, M.-H.; Park, H.B.; Kim, C.-M.; Song, J.-h.; Kim, I.S. Tunable semi-permeability of graphene-based membranes by adjusting reduction degree of laminar graphene oxide layer. *J. Membr. Sci.* **2018**, *547*, 73–79. [[CrossRef](#)]
48. Ambrosi, A.; Pumera, M. Electrochemically exfoliated graphene and graphene oxide for energy storage and electrochemistry applications. *Chem. A Eur. J.* **2016**, *22*, 153–159. [[CrossRef](#)]
49. Cao, J.; He, P.; Mohammed, M.A.; Zhao, X.; Young, R.J.; Derby, B.; Kinloch, I.A.; Dryfe, R.A. Two-step electrochemical intercalation and oxidation of graphite for the mass production of graphene oxide. *J. Am. Chem. Soc.* **2017**, *139*, 17446–17456. [[CrossRef](#)]
50. Zhang, L.; Zhang, Z.; He, C.; Dai, L.; Liu, J.; Wang, L. Rationally designed surfactants for few-layered graphene exfoliation: Ionic groups attached to electron-deficient π -conjugated unit through alkyl spacers. *ACS Nano* **2014**, *8*, 6663–6670. [[CrossRef](#)]
51. Wang, H.; Wei, C.; Zhu, K.; Zhang, Y.; Gong, C.; Guo, J.; Zhang, J.; Yu, L.; Zhang, J. Preparation of graphene sheets by electrochemical exfoliation of graphite in confined space and their application in transparent conductive films. *ACS Appl. Mater. Interfaces* **2017**, *9*, 34456–34466. [[CrossRef](#)] [[PubMed](#)]
52. Eigler, S.; Enzelberger-Heim, M.; Grimm, S.; Hofmann, P.; Kroener, W.; Geworski, A.; Dotzer, C.; Röckert, M.; Xiao, J.; Papp, C. Wet chemical synthesis of graphene. *Adv. Mater.* **2013**, *25*, 3583–3587. [[CrossRef](#)] [[PubMed](#)]
53. Szabó, T.; Berkesi, O.; Forgó, P.; Josepovits, K.; Sanakis, Y.; Petridis, D.; Dékány, I. Evolution of surface functional groups in a series of progressively oxidized graphite oxides. *Chem. Mater.* **2006**, *18*, 2740–2749. [[CrossRef](#)]
54. Jeong, H.-K.; Lee, Y.P.; Lahaye, R.J.; Park, M.-H.; An, K.H.; Kim, I.J.; Yang, C.-W.; Park, C.Y.; Ruoff, R.S.; Lee, Y.H. Evidence of graphitic AB stacking order of graphite oxides. *J. Am. Chem. Soc.* **2008**, *130*, 1362–1366. [[CrossRef](#)]
55. Achee, T.C.; Sun, W.; Hope, J.T.; Quitzau, S.G.; Sweeney, C.B.; Shah, S.A.; Habib, T.; Green, M.J. High-yield scalable graphene nanosheet production from compressed graphite using electrochemical exfoliation. *Sci. Rep.* **2018**, *8*, 14525. [[CrossRef](#)]
56. Lin, X.; Shen, X.; Zheng, Q.; Yousefi, N.; Ye, L.; Mai, Y.-W.; Kim, J.-K. Fabrication of Highly-Aligned, Conductive, and Strong Graphene Papers Using Ultralarge Graphene Oxide Sheets. *ACS Nano* **2012**, *6*, 10708–10719. [[CrossRef](#)]
57. Koenig, S.P.; Boddeti, N.G.; Dunn, M.L.; Bunch, J.S. Ultrastrong adhesion of graphene membranes. *Nat. Nanotechnol.* **2011**, *6*, 543–546. [[CrossRef](#)]
58. Sanchez, D.A.; Dai, Z.; Wang, P.; Cantu-Chavez, A.; Brennan, C.J.; Huang, R.; Lu, N. Mechanics of spontaneously formed nanoblisters trapped by transferred 2D crystals. *Proc. Natl. Acad. Sci. USA* **2018**, *115*, 7884–7889. [[CrossRef](#)]
59. Suk, J.W.; Na, S.R.; Stromberg, R.J.; Stauffer, D.; Lee, J.; Ruoff, R.S.; Liechti, K.M. Probing the adhesion interactions of graphene on silicon oxide by nanoindentation. *Carbon* **2016**, *103*, 63–72. [[CrossRef](#)]
60. Semoto, T.; Tsuji, Y.; Tanaka, H.; Yoshizawa, K. Role of Edge Oxygen Atoms on the Adhesive Interaction between Carbon Fiber and Epoxy Resin. *J. Phys. Chem. C* **2013**, *117*, 24830–24835. [[CrossRef](#)]
61. Megra, Y.T.; Suk, J.W. Adhesion properties of 2D materials. *J. Phys. D Appl. Phys.* **2019**, *52*, 364002. [[CrossRef](#)]
62. Na, S.R.; Kim, Y.; Lee, C.; Liechti, K.M.; Suk, J.W. Adhesion and Self-Healing between Monolayer Molybdenum Disulfide and Silicon Oxide. *Sci. Rep.* **2017**, *7*, 14740. [[CrossRef](#)]